



Cross-linked ultrathin polyphosphazene-based nanosheet with promoted charge separation kinetics for efficient visible light photocatalytic CO₂ reforming to CH₄

Guoen Tang^a, Xiangdong Zeng^a, Linquan Hou^a, Ting Song^{a,*}, Shiheng Yin^b, Bei Long^a, Atif Ali^c, Guo-Jun Deng^{a,*}

^a Key Laboratory for Green Organic Synthesis and Application of Hunan Province, Key Laboratory of Environmentally Friendly Chemistry and Application of Ministry of Education, College of Chemistry, Xiangtan University, Xiangtan 411105, China

^b Analytical and Testing Center, South China University of Technology, Guangzhou 510640, China

^c Department of Chemistry and State Key Laboratory of Synthetic Chemistry, The University of Hong Kong, Pokfulam Road, Hong Kong, China

ARTICLE INFO

Keywords:

Cross-linked structure
Polyphosphazene-based
CO₂ reduction
High selectivity
Visible light

ABSTRACT

Organic polymer materials as a promising type of photocatalyst are still limited by the poor transport efficiency of photoinduced carrier. Herein, a series of cross-linked ultrathin polyphosphazene-based nanosheets is developed by regulating the N-containing skeleton. The aromatic ring, pyrimidine ring and s-triazine ring are bonded with cyclotriphosphazene to form large-sized 2D nanosheets, respectively. Experimental results and theoretical calculations have determined the pyrimidine ring that has a stronger ability to adsorb CO₂ and can provide a suitable band gap and a stronger built-in electric field, so as to realize the rapid separation of photoproduced carrier. 2PC sample with the pyrimidine ring delivered near 100% selectivity for CO₂-to-CH₄ conversion with an impressive rate of 626 μmol g⁻¹ without cocatalyst and photosensitizer under visible light illumination, surpassing many reported photocatalysts. Briefly, this work offers a fresh means for the construction of high-performance polymers by regulating the internal framework.

1. Introduction

Excessive carbon dioxide (CO₂) emissions have clearly harmed the environment and prompted the use of photocatalysis to convert CO₂ into high value-added chemicals [1,2]. In order to optimize the activity and selectivity of CO₂ reduction, a wide range of carbon materials, metal organic complexes and metal oxides have been explored [3]. Among various CO₂ reduction products such as CH₃OH, CO, HCOOH and CH₄, CH₄ is a widely used chemical raw material and fuel [4,5]. In particular, the photocatalytic reduction of CO₂ to CH₄ may be scaled up to achieve sustainable natural gas production [6]. As we all know, compared to the more common CO products only need two electrons, CH₄ not only requires to overcome the strong dissociation energy of the C-O bond (~750 kJ), but also captures eight electrons to participate in the reaction [7,8]. Therefore, the realization of photocatalysts for selective photo-reduction of CO₂ to CH₄ requires stronger photon capture ability, significant absorption of CO₂ molecules, and the fast separation of photogenerated carrier.

As an alternative material, organic copolymers have attracted widespread attention because of their obvious advantages, such as electronic properties controlled by synthesis, finely adjustable structure and low toxicity [9]. The reported polymer photocatalysts mainly include covalent organic framework, covalent triazine framework and graphite carbon nitride polymer [10,11]. In recent years, cross-linked polyphosphazenes with abundant heteroatoms and stable covalent frameworks have received extensive attention [12,13]. The organic monomers with double/multiple nucleophilic groups are connected with cyclotriphosphazene due to nucleophilic substitution and a cross-linked matrix is produced through a one-step precipitation polycondensation [14]. Using different monomers, such as fluorescein, melamine and 4,4'-(hexafluoroisopropylidene) diphenol, the obtained polymer can be endowed with different characteristics, making it a potential candidate for photocatalyst (stronger light absorption and enlarged reaction surface) [15,16]. However, the rapid recombination of photogenerated carriers in the currently prepared cross-linked polymers results in extremely low photocatalytic activity.

* Corresponding authors.

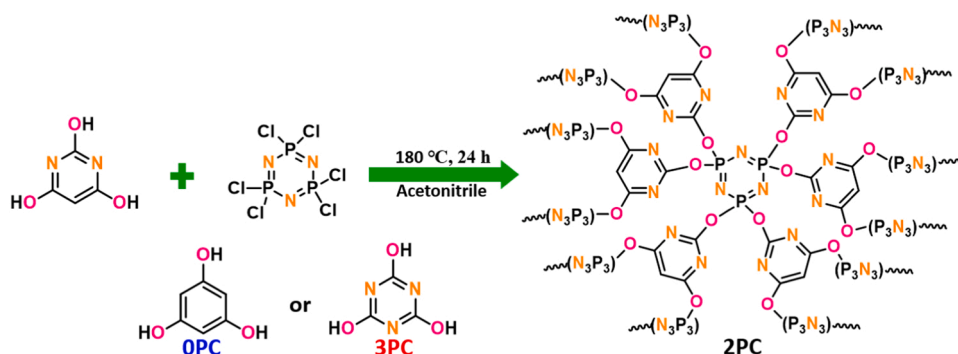
E-mail addresses: songtg@xtu.edu.cn (T. Song), gjdeng@xtu.edu.cn (G.-J. Deng).

<https://doi.org/10.1016/j.apcatb.2022.121090>

Received 24 October 2021; Received in revised form 29 December 2021; Accepted 8 January 2022

Available online 11 January 2022

0926-3373/© 2022 Elsevier B.V. All rights reserved.



Scheme 1. Illustration of the synthetic process of cross-linked ultrathin polyphosphazene-based nanosheet.

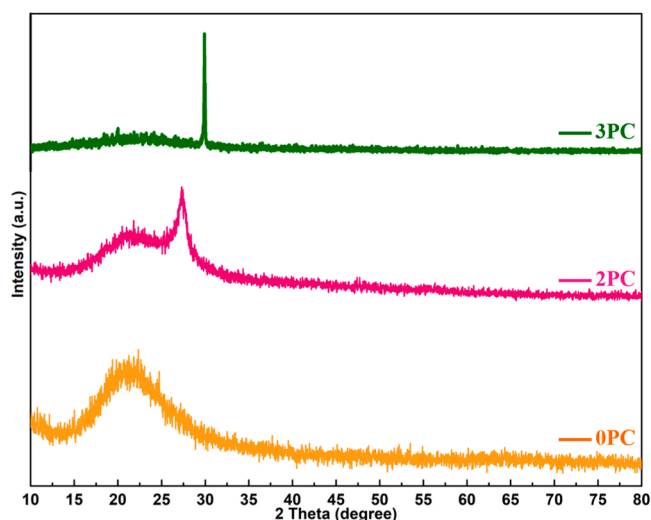


Fig. 1. XRD patterns of 0PC, 2PC and 3PC samples.

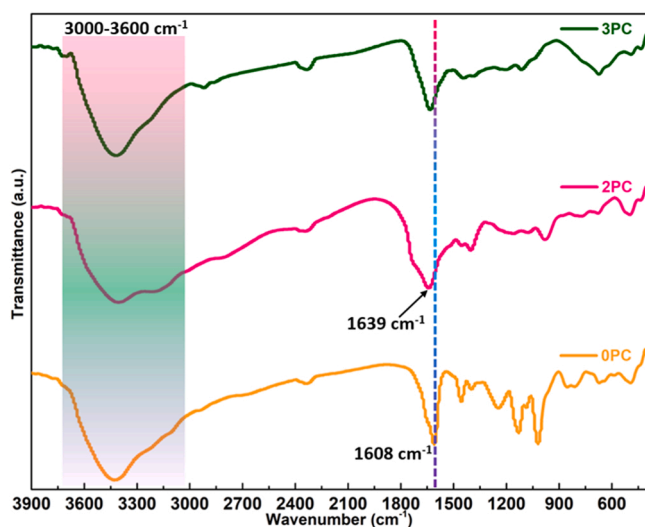


Fig. 2. FTIR spectra of 0PC, 2PC and 3PC samples.

Among many control strategies, choosing a suitable monomer structure can promote the separation of photogenerated carriers in the polymer photocatalyst [17]. Many studies have proved that the N-containing framework can control the energy levels of the dipole and the molecular pre-orbital, thereby adjusting the built-in electric field and energy band of a photocatalyst [18,19]. Moreover, the implantation of

N-containing framework not only prolongs the life of photoinduced carriers, but also produces strong lewis basicity, which is beneficial to the adsorption of CO₂ [20]. Therefore, fine-tuning the N-containing framework in the cross-linked polyphosphazene-based material will synergistically solve the sufficient capture of photons, the adsorption of CO₂ molecules, and the rapid separation of photogenerated carriers, thereby significantly improving the photocatalytic activity. However, there are no reports that pay attention to the structure of the polymer itself, especially only adjusting its N-containing skeleton to significantly affect its photocatalytic activity.

In this work, we have carefully designed a new type of cross-linked ultrathin polyphosphazene-based nanosheets with different N-containing skeletons (aromatic ring, pyrimidine ring and s-triazine ring) through a facile synthesis method. 2PC nanosheet with pyrimidine ring performs remarkable CH₄ generation ability (626 μmol g⁻¹) with a high selectivity of near 100% under visible light irradiation. The acquired results prove that the photocatalytic activity of as-produced polymer significantly depends on the structure of the monomer, which effectively improves the polymer's photon capture performance, built-in electric field and CO₂ adsorption capacity. These results highlight the opportunity of cross-linked ultrathin polyphosphazene-based nanosheets for diverse transformations.

2. Experimental section

2.1. Preparation of cross-linked ultrathin polyphosphazene-based nanosheet

Cross-linked ultrathin polyphosphazene-based nanosheet was acquired by a facile synthesis method. Typically, 2 mmol of hexachlorocyclotriphosphazene, 50 mL of CH₃CN and 6 mmol of barbituric acid were placed in a 100 mL autoclave. The solution was stirred overnight, and then the autoclave was maintained to 180 °C for 24 h. The obtained powders were cleaned alternately with absolute ethanol and distilled water. The final powders were obtained after being dried at 50 °C in vacuum overnight, marked as 2PC. Similarly, 0PC and 3PC samples have been obtained by replacing the barbituric acid with phloroglucinol and cyanuric acid, respectively, but the other synthetic steps are the same.

2.2. Characterization

The XRD patterns of catalysts were collected on a Bruker D8 Focus Diffractometer with Cu Kα radiation. The morphologies of as-obtained samples were explored on an electron microscope (TEM-2100 F, Japan). N₂ adsorption-desorption isotherms were performed at 77 K using Micromeritics ASAP Tri-star II 3020 equipment. The composition and electronic state were recorded by X-ray photoelectron spectroscopy (XPS, Axis Ultra DLD, Kratos). Thermogravimetric analysis was detected with a Mettler TG50 instrument under air flow at heating rate of 10 °C

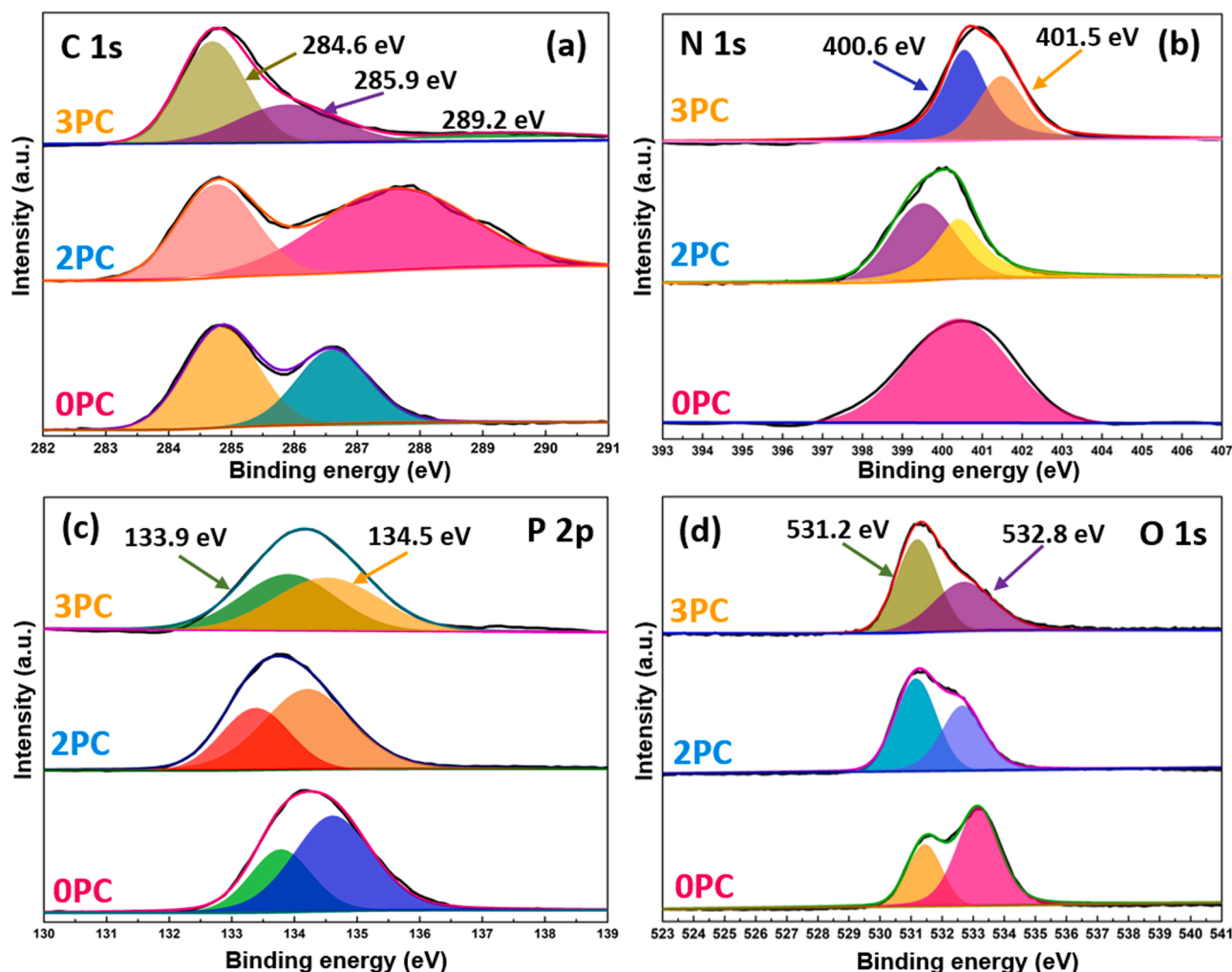


Fig. 3. High-resolution XPS spectrum of OPC, 2PC and 3PC samples under study: (a) C 1 s, (b) N 1 s, (c) P 2p, and (d) O 1 s.

min^{-1} in the range 30–670 °C. UV–vis diffuse reflectance spectrum (DRS) was obtained on a UV–vis spectrophotometer (UV-3600, Shimadzu, Japan) with BaSO_4 as a reference. Steady-state/time-resolved photoluminescence (PL) emission spectra were investigated with a fluorescence spectrophotometer (Edinburgh Instruments, FLSP-920). CH_4 labelled by ^{13}C was performed with gas chromatography-mass spectrometer (Agilent 6890 N/5975, USA).

2.3. Photocatalytic performance measurements

The photocatalytic performances of as-acquired catalysts were measured in a Pyrex reactor with good air tightness. In a typical process, 5 mg catalyst was dispersed with a magnetic stirrer in a 100 mL Pyrex reactor (2 mL H_2O , 3 mL CH_3CN and 1 mL TEOA). The reactor was vacuumed, and then 1 atm CO_2 pumped in. Afterwards, the reactor was illuminated under a 300 W Xe lamp with a UV cutoff filter ($>420\text{ nm}$). The products were analyzed via using gas chromatography (GC7900, Tian Mei, Shanghai) equipped with FID detector for CO and CH_4 detections and TCD detector for H_2 detection.

2.4. Electrochemical analysis

CHI660E electrochemical workstation with a standard three-electrode system was employed to measure the electrochemical properties of as-obtained catalysts, in which working electrode, reference electrode and counter electrode were sample electrode, Ag/AgCl

electrode and platinum tablet with 0.1 M Na_2SO_4 solution, respectively. The sample electrodes were acquired as follows: 50 mg of catalyst were added in 1 mL of anhydrous ethanol to generate a slurry. Next, the slurry was coated onto fluorine doped stannic oxide glass through the doctor blade method.

3. Results and discussion

3.1. Composition and structure

The cross-linked ultrathin polyphosphazene-based nanosheets were synthesized by the solvothermal reaction of hydroxyl and phosphorus chloride groups at 180 °C for 24 h (Scheme 1). The two monomers in 2PC are connected by a single ether bond to produce a single-chain connection mode. Moreover, one hexachlorocyclotriphosphazene can form six ether bonds, and as it continues to expand, a huge cross-linking network will be formed. In order to control its N-containing skeleton, the aromatic ring and s-triazine ring were replaced with pyrimidine ring to explore its impact on photocatalytic activity. Fig. 1 shows the XRD spectra of OPC, 2PC and 3PC samples with different N-containing skeletons. OPC sample displays an amorphous structure. With the introduction of pyrimidine ring, 2PC sample showed a broad (002) peak at 27.4° , which corresponds to the periodic stacking of conjugated systems [21]. 3PC sample displays a strong diffraction peak at 29.8° , which was obviously attributed to the implantation of s-triazine ring. From a subtle point of view, the gradual increase in N content will obviously affect its

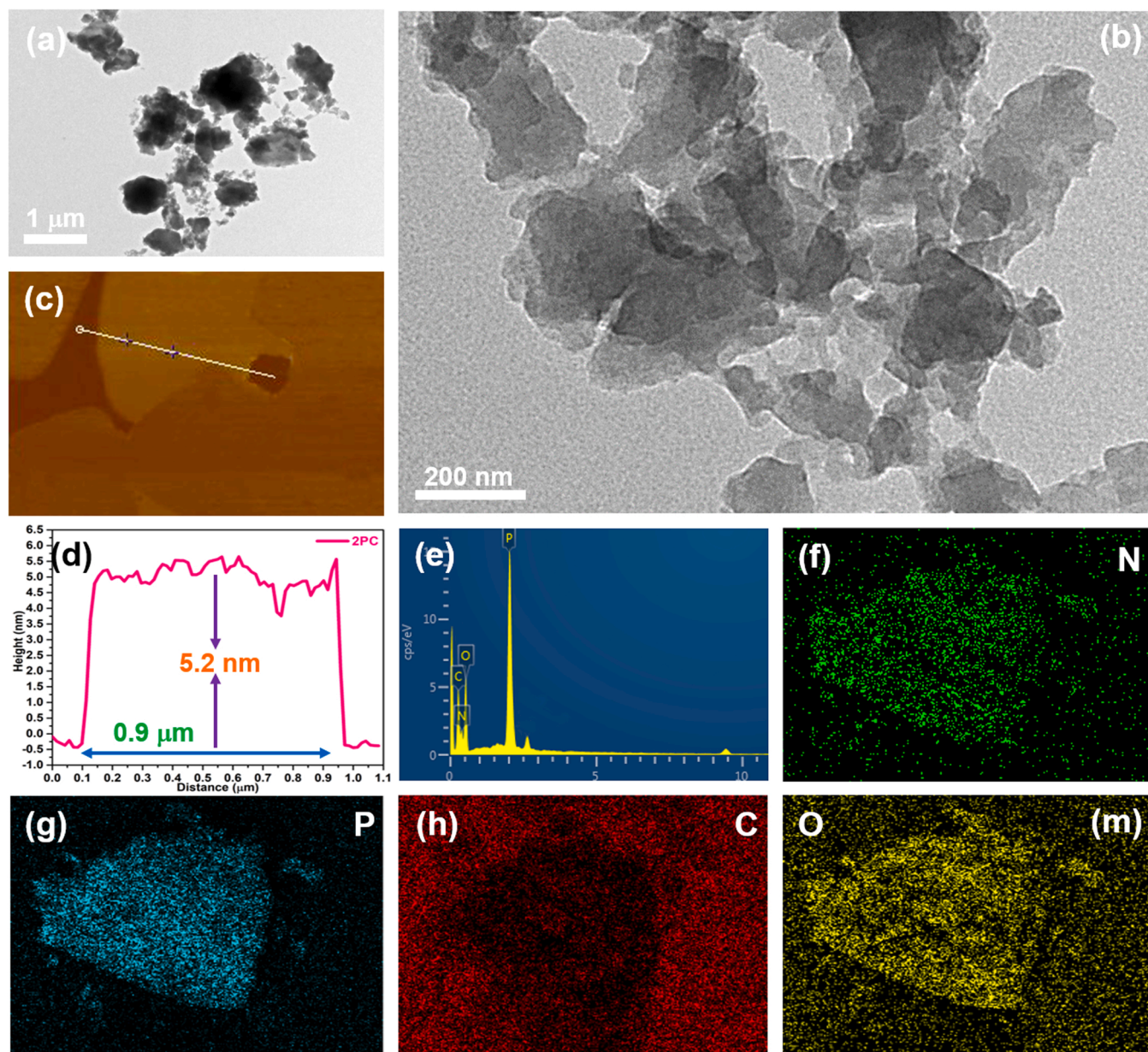


Fig. 4. TEM images (a and b) of 2PC sample. AFM image (c) and height cutaway view (d) of 2PC. EDS spectrum (e) of 2PC. Elemental mappings of N (f), P (g), C (h) and O (m) for 2PC.

crystallinity, which is similar to other N-doped materials [22,23]. The internal structure of OPC, 2PC and 3PC samples was also studied by FTIR test. Fig. 2 indicates that OPC sample at 1608 cm^{-1} is due to $\text{C}=\text{C}$ in the aromatic ring, which comes from the aromatic ring [24]. The peak at 1639 cm^{-1} is assigned to the $\text{C}=\text{N}$ bond, which explains the pyrimidine ring in 2PC sample and the s-triazine ring in 3PC sample, respectively [25]. Moreover, the peak at 1038 cm^{-1} is designed as the P-O bond, which fully demonstrates that ultrathin polyphosphazene-based nanosheets are connected by ether bonds [26]. The peak at 1200 cm^{-1} in as-prepared sample is ascribed to the $\text{P}=\text{N}$ bond of cyclotriphosphazene [27]. The broad peaks at $3000\text{--}3600\text{ cm}^{-1}$ are ascribed to the O-H stretching vibration of C-OH, which originates from unreacted hydroxyl functional group [28,29]. For Raman spectra (Fig. S1), the bands of $142\text{--}340\text{ cm}^{-1}$ in the 2PC samples are assigned to vibrations of the cyclotriphosphazene. It can be clearly observed that the Raman spectra of the OPC and 3PC samples have peak shifts and reduced peaks, which once again shows that the skeleton structure is affected by other two rings. Moreover, the band at 470 cm^{-1} associated with the breathing

modes of the s-triazine ring in 3PC sample, whereas the peaks at 989 cm^{-1} are designed with the stretching modes of the pyrimidine ring in 2PC sample [30,31]. The above results fully illustrate that ultrathin polyphosphazene-based nanosheets with different N-containing frameworks were prepared via using a facile synthesis method. TG analysis was used to study the thermal properties of two monomers and 2PC samples, and the curves obtained are shown in Fig. S2. The weights of cyclotriphosphazene and barbituric acid are thermally degraded to about 0 wt% at $160\text{ }^{\circ}\text{C}$ and $680\text{ }^{\circ}\text{C}$, respectively. After cross-linking, the thermal stability of 2PC sample was significantly improved ($680\text{ }^{\circ}\text{C}$, 48.2 wt%).

The surface chemical compositions of OPC, 2PC and 3PC samples were recorded via using XPS spectra. For 3PC sample, the C 1s peak (Fig. 3a) can be fitted to 289.2, 285.9, and 284.6 eV, which are the C-O band, N-bonded sp^2 C atom in $\text{N}-\text{C}=\text{N}$, and foreign hydrocarbon of the XPS instrument itself, respectively [32,33]. When the pyrimidine ring is used to replace the s-triazine ring, the binding energy of C 1s peak in 2PC sample is obviously red-shifted. The peaks of N 1s (Fig. 3b) at

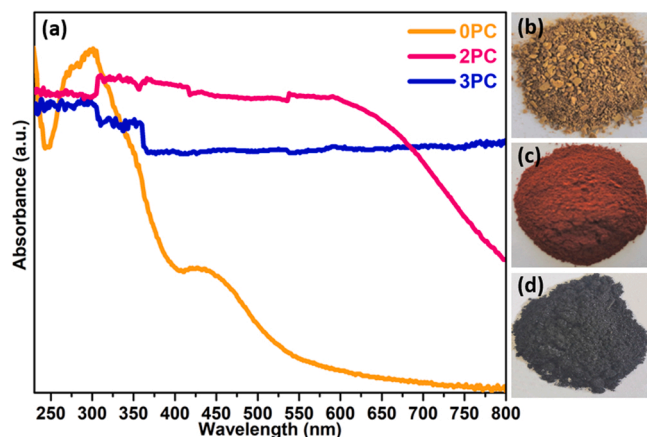


Fig. 5. (a) UV-vis diffuse reflectance spectra (DRS) of OPC, 2PC and 3PC samples. Photographs of (b) OPC, (c) 2PC and (d) 3PC samples.

400.6 eV and 401.5 eV are attributed to the $P=N$ and $C=N$, respectively [34]. Two peaks at 133.9 and 134.5 eV can be detected in the XPS spectrum of P 2p (Fig. 3c), which are respectively attributed to the P-O and N-P=N bond, certifying that cyclotriphosphazene does exist in ultrathin nanosheets [35]. As shown in O 1s spectrum (Fig. 3d), there

are two O species in as-produced samples, with binding energies of 531.2 (for C-O) and 532.8 eV (for P-O) derived from the ether bond connecting the two monomers [36]. XPS results clearly prove that ultrathin polyphosphazene-based nanosheets with different N-containing skeletons were successfully prepared through a facile synthesis strategy.

A nanosheet-type structure of 2PC sample was probed by TEM and AFM analysis. As shown in Fig. 4a and b, the nanosheet domains are very thin and large-sized 2D structures. The AFM image (Fig. 4c and d) further confirms that the thickness of these nanosheets is about 5.2 nm, which clearly shows that the 2D nanosheets are ultrathin structures. This result indicates that without any post-treatment measures, only a simple cross-linking process can be used to obtain ultrathin polyphosphazene-based nanosheets. The EDS (Fig. 4e) and element mapping are displayed in Fig. 4f-m, and the main elements of 2PC sample are C, N, O and P. The cross-linked ultrathin polyphosphazene-based nanosheet can be clearly seen from the above characterization. The BET surface areas of as-acquired samples were also measured and presented in Fig. S3. The BET surface area of OPC ($21.8 \text{ m}^2 \text{ g}^{-1}$) is greater than that of 2PC sample ($10.7 \text{ m}^2 \text{ g}^{-1}$) and 3PC sample ($11.1 \text{ m}^2 \text{ g}^{-1}$).

3.2. Optical property

Fig. 5 displays the UV-vis absorption spectra of OPC, 2PC and 3PC samples. The absorption edge of OPC is $\sim 435 \text{ nm}$, which corresponds to the band gap of $\sim 2.85 \text{ eV}$ according to the Kubelka-Munk function.

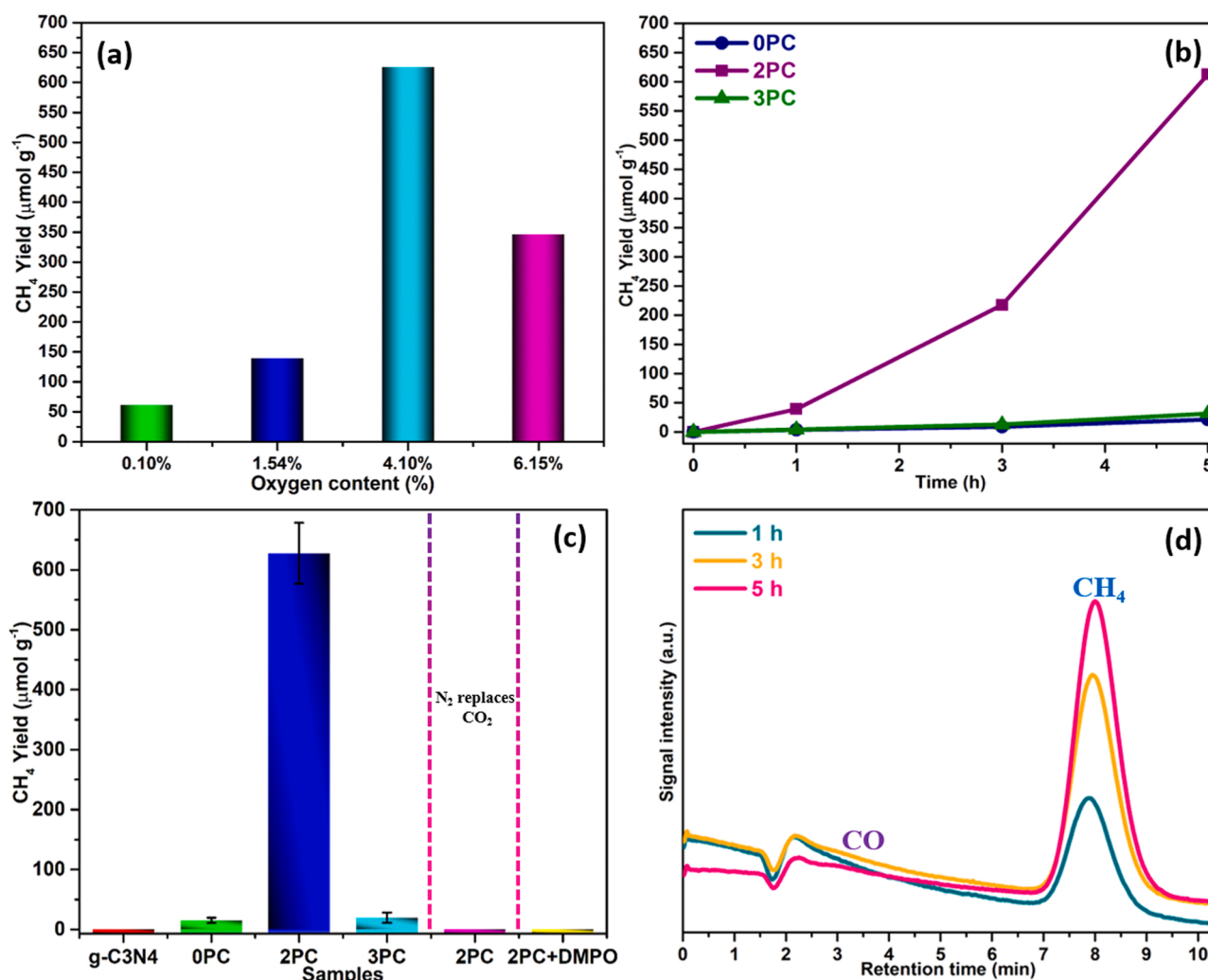


Fig. 6. Photocatalytic CO_2 reduction activity: (a) the 2PC sample modified with different volume ratios of O_2 ; (b) Photocatalytic CO_2 evolution curves over OPC, 2PC and 3PC samples; (c) the various bimetals (g- C_3N_4 , OPC, 2PC and 3PC samples). (d) GC Chromatogram of CO and CH_4 accumulated for 5 h by the 2PC sample.

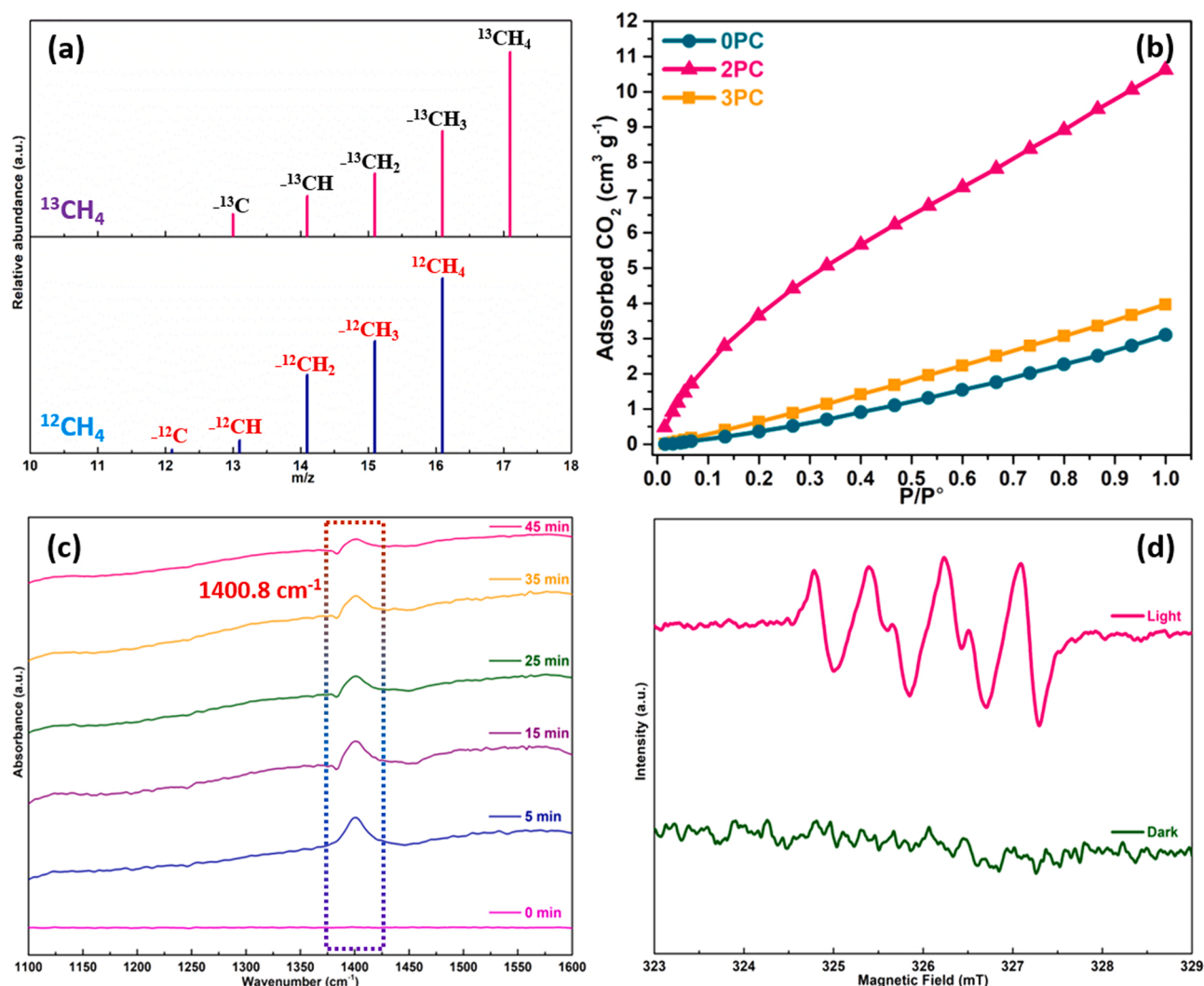


Fig. 7. (a) Mass spectra of $^{13}\text{CH}_4$ ($m/z = 17$) produced over 2PC sample. (b) CO_2 adsorption capacities of 0PC, 2PC and 3PC samples. (c) In situ FT-IR spectra of CO_2 adsorption on 2PC sample. (d) ESR spectra of O_2^- in 2PC sample.

Moreover, the absorption spectrum of 0PC sample shows a broad peak at 439 nm because the cyclotriphosphazene is conjugated with the aromatic ring to construct a new delocalized electronic state, called the middle band gap state. In addition, 2PC sample exhibits a broad and strong visible light absorption because the pyrimidine ring is substituted for the aromatic ring. 3PC sample further displayed obvious visible light absorption along with the s-triazine ring, and even extended to near-infrared light absorption, which matches the appearance color of 3PC sample. The band gap (E_g) of 2PC sample acquired from the Kubelka-Munk means is 1.51 eV (Fig. S4a) [37]. The XPS valence band (VB) spectra are further measured to elucidate the VB positions of 2PC sample [38]. As shown in Fig. S4b, the VB level of 2PC samples was + 1.03 eV. Combined with the above band gap, the CB position of 2PC sample was - 0.48 eV. The above facts show that 2PC sample meets the thermodynamic requirements in the process of photoreduction CO_2 to CH_4 ($E_{\text{CH}_4/\text{CO}_2} = -0.24$ eV) [39].

3.3. CO_2 reduction result

The photocatalytic CO_2 reduction for as-obtained samples was tested under visible light illumination without cocatalyst and photosensitizer. Interestingly, we found that low levels of oxygen (O_2) act a key role in the photocatalytic CO_2 reduction (Fig. 6a). As the O_2 content increases, the CH_4 evolution rate of 2PC sample gradually improves. Once the

content exceeds 4.10%, the activity of 2PC sample is greatly inhibited. Under the optimal O_2 content, 2PC sample showed the best CH_4 emission rate of 626 $\mu\text{mol g}^{-1}$. Moreover, it can be clearly seen that the CH_4 production rates of 0PC, 2PC and 3PC sample increase with time (Fig. 6b). The CH_4 evolution rate of 2PC sample is 626 $\mu\text{mol g}^{-1}$, which is 40.6 and 31.8 times than that of 0PC sample (15.4 $\mu\text{mol g}^{-1}$) and 3PC (19.7 $\mu\text{mol g}^{-1}$), respectively (Fig. 6c). Under the same conditions, g- C_3N_4 sample does not detect CH_4 activity. In order to explore the carbon source, 2PC sample did not detect any CH_4 content after replacing CO_2 with N_2 . Moreover, the photocatalytic activity of 2PC sample was also tested under different wavelengths of irradiation. As presented in the Fig. S5, as the wavelength of monochromatic light increases, the CH_4 yield of 2PC sample gradually decreases, which shows that the energy of monochromatic light is very important for the production of CH_4 . In order to clarify the role of O_2 , we used a superoxide radical trap ($\cdot\text{O}_2^-$). The results indicated that 2PC sample also did not show any CH_4 evolution rate. The original gas spectrum is provided to further verify the selectivity of photocatalytic CO_2 reduction (Fig. 6d). It can be clearly seen that only the peak of CH_4 appears, but the peak of CO does not emerge. Similarly, H_2 is also not detected. This fully displays that the CH_4 yield is close to near 100%, which will greatly benefit the subsequent purification process, thereby significantly reducing potential costs. An isotope tracer analysis was performed to confirm that CH_4 was produced by CO_2 photoreduction, which was performed under the

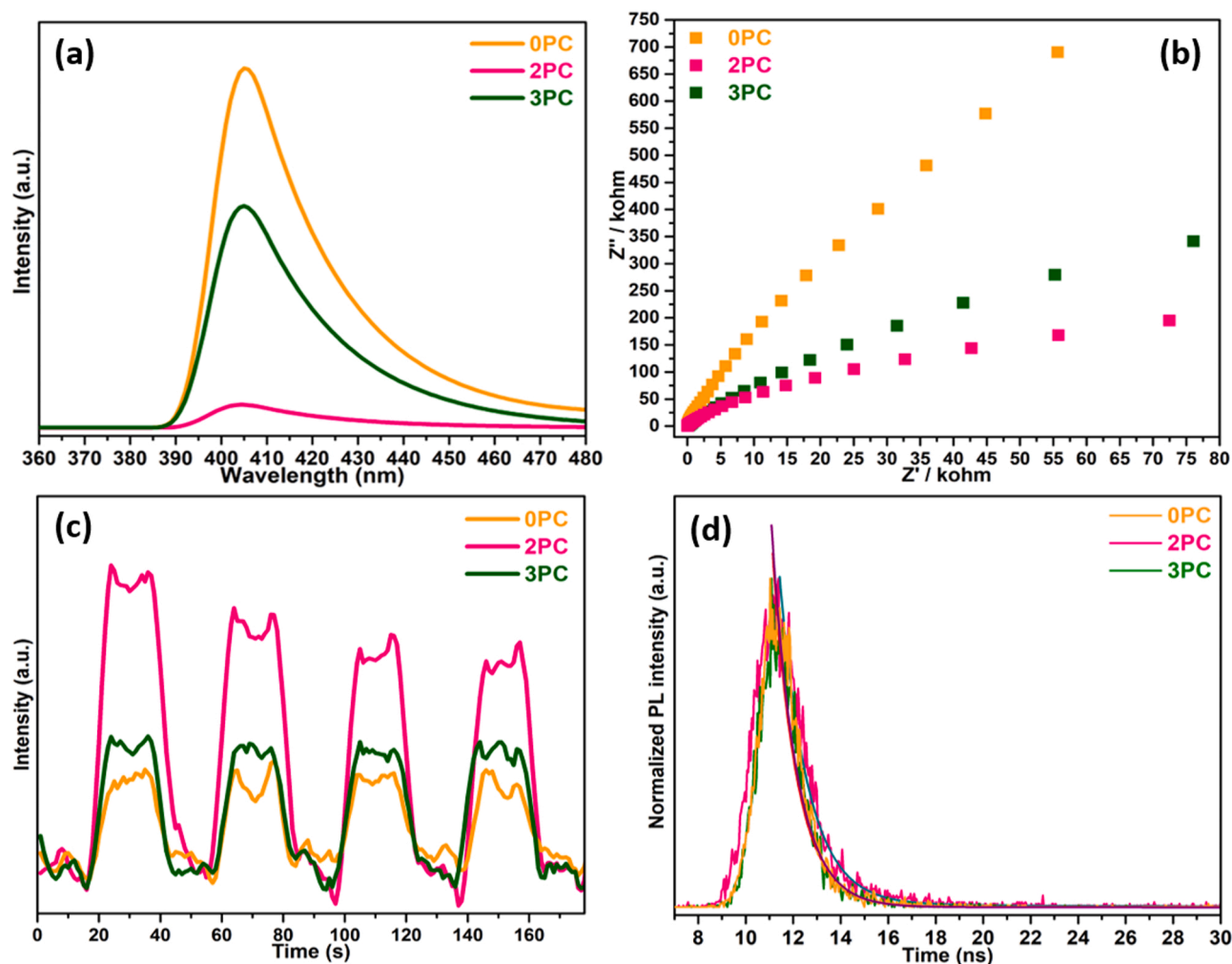


Fig. 8. (a) Steady-state photoluminescence (PL) spectra of OPC, 2PC and 3PC samples. (b) Electrochemical impedance spectra (EIS) of OPC, 2PC and 3PC samples. (c) Transient photocurrent responses of OPC, 2PC and 3PC samples. (d) Time-resolved PL decay profiles for OPC, 2PC and 3PC samples.

condition of replacing $^{13}\text{CO}_2$ with $^{12}\text{CO}_2$ (Fig. 7a). The GC-MS result is designated as $^{13}\text{CH}_4$ ($m/z = 17$), which indicates that the carbon source of CH_4 comes from CO_2 . Five cycles of testing have verified the stability of 2PC sample and can maintain a high yield (Fig. S6). The XRD, XPS and FTIR characterization (Figs. S7–9) of 2PC sample before and after the reaction proved the stability of its structure.

3.4. Clarification of the proposed mechanism

The higher affinity of photocatalyst for CO_2 molecules will obviously benefit the surface reduction reaction. Once the CO_2 is fixed through the the surface of adsorption sites in as-acquired samples, its can be converted into CH_4 in cooperation with photoelectrons [40]. The CO_2 adsorption capacity (Fig. 7b) at the pressure ($P/P^0 = 1.0$) of 2PC sample is $10.6 \text{ cm}^3 \text{ g}^{-1}$, which is 3.4 and 2.7 folds than that of OPC ($3.1 \text{ cm}^3 \text{ g}^{-1}$) and 3PC ($4.0 \text{ cm}^3 \text{ g}^{-1}$). Interestingly, compared with OPC sample, although the introduction of pyrimidine ring lead to an obvious decrease in the specific surface area of 2PC sample, it constructed effective adsorption sites to overcome the adverse effects of low surface area, thereby significantly improving the ability to adsorb CO_2 molecules [41].

In-situ FTIR spectroscopy can detect the subtle process of photocatalytic CO_2 reduction [42]. As depicted in Fig. 7c, before the light irradiation, with the existence of H_2O and CO_2 in the reaction system, there is no infrared peak. Once the light is started, 2PC sample displays a strong peak at 1400.8 cm^{-1} , which is designed as the HCO_3^- group.

This group is generally considered to be the initial intermediate for the photoreduction of CO_2 to CH_4 . With the prolongation of illumination time, the corresponding peaks gradually decrease. This indicates that the rapid production of acquired CH_4 consumes more reaction intermediates. Electron spin resonance measurement (ESR) is used to explore the role of O_2 in the reduction process (Fig. 7d) [43]. In the dark, no O_2^- signal was found. A characteristic peak of O_2^- appears after visible light illumination. Combined with free radical capture experiments, it has been confirmed that O_2^- is the main active specie.

The PL technology was used to study the migration process of photogenerated carriers in as-acquired samples [44]. As shown in Fig. 8a, due to the rapid recombination of photoproduct carrier generated by OPC sample, the fluorescence emission spectrum of OPC sample has a maximum emission peak at 405 nm, which has a strong wide range (385–460 nm). The intensity of fluorescence spectrum in 3PC sample at 405 nm is slightly reduced because the s-triazine ring is implanted in the polymer framework, which can obvious enhance the separation of photoinduced carriers. Furthermore, the fluorescence intensity of 2PC sample was significantly lower than that of OPC and 3PC sample only because the monomer was replaced with the pyrimidine ring. The above results fully confirm that regulating N-containing framework can significantly affect the transmission of photoinduced carriers, thereby improving its photocatalytic activity.

In order to clarify the mechanism of enhanced photocatalytic activity, the charge separation efficiency was studied by electrochemical impedance spectroscopy (EIS) [45]. The arc radius of impedance

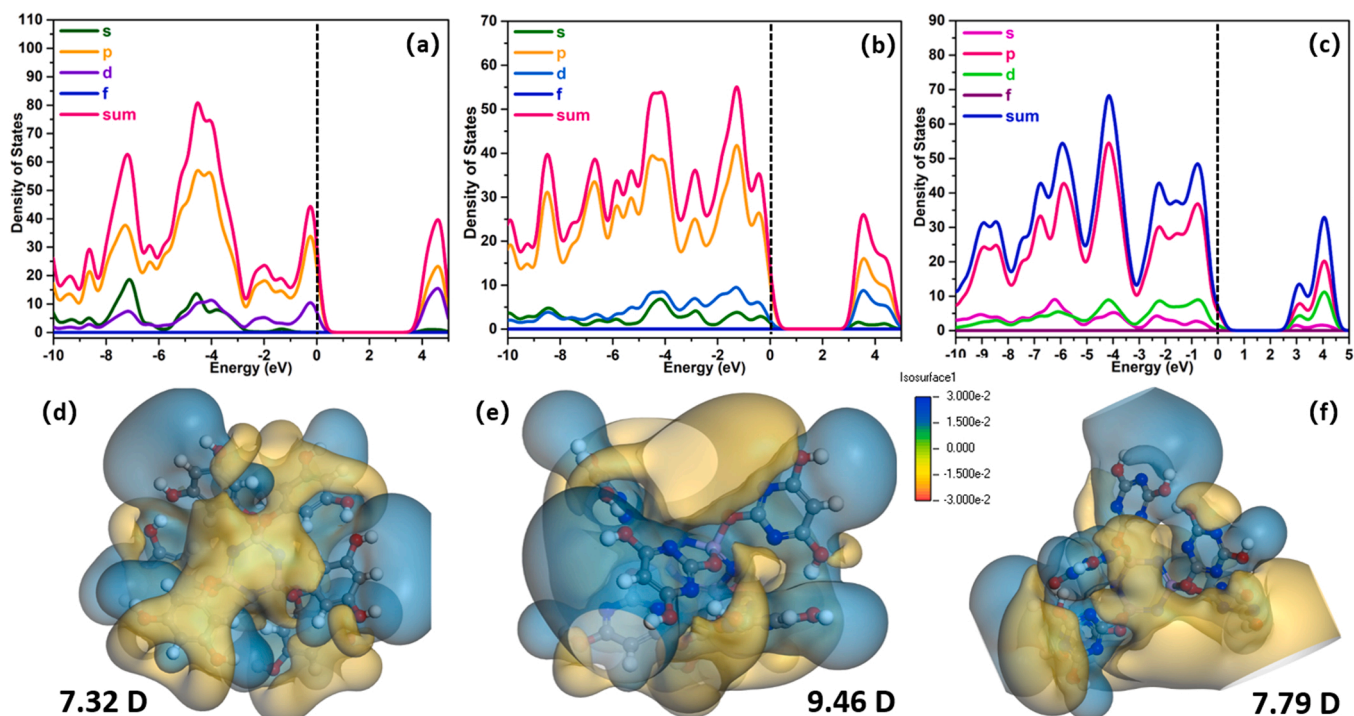


Fig. 9. Density of states of OPC (a), 2PC (b) and 3PC (c) samples. The ESP and molecular dipole of OPC (d), 2PC (e) and 3PC (f) samples. The results were calculated by DFT, b3lyp, 6–311 g.

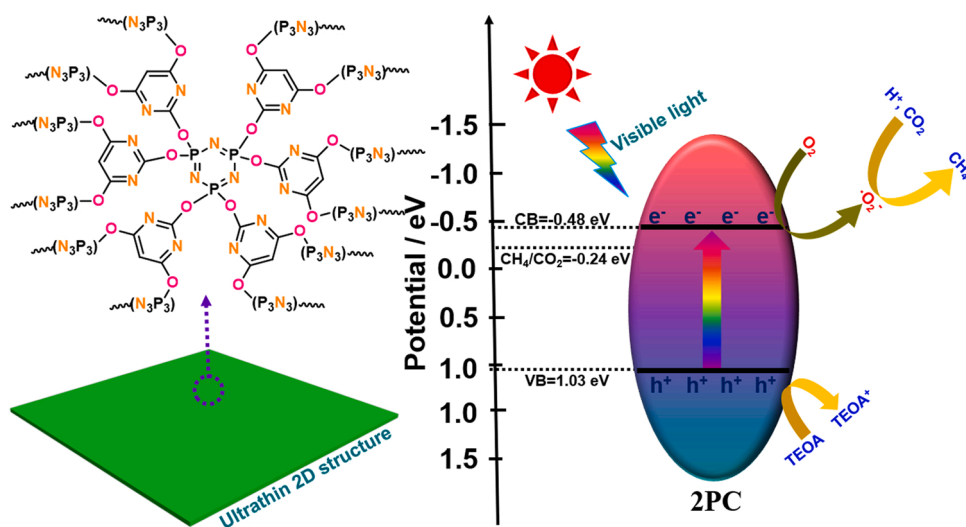


Fig. 10. A possible mechanism for photocatalytic CO₂ reduction about 2PC sample.

spectrum is consistent with the impedance value (Fig. 8b). Correspondingly, the separation efficiency of photoinduced carriers in photocatalyst becomes lower as the resistance value is higher. In addition, the resistance of 2PC sample is lower than that of the OPC and 3PC samples, showing that the separation of photoproduct carriers in 2PC sample is better than that of OPC and 3PC samples. Therefore, the implantation of pyrimidine ring in the skeleton of ultrathin nanosheets can significantly promote the separation and migration of photoinduced carrier at the interface to greatly improve the photocatalytic activity.

The charge separation efficiency of as-acquired samples was studied by photoelectrochemical (PEC) method [46]. Fig. 8c confirms the transient photocurrent response (*i-t*) curves recorded for OPC, 2PC and 3PC samples under visible light illumination. Among them, 2PC sample displays a significantly higher photocurrent density compared to 3PC

and OPC sample, which means that the ultrathin nanosheet with pyrimidine ring can significantly promote the interface charge transfer. Therefore, more photoexcited carriers may contribute to the production of CH₄. In order to further explore the charge transfer kinetics, the transient fluorescence spectra of as-acquired samples were studied [47]. The electrons inside the material are excited via using absorb photons and then transition to an excited state. As shown in Fig. 8d, 2PC displays long ($\tau_1 = 1.48$ ns, 75.0%) and short ($\tau_2 = 10.32$ ns, 25.0%) lifetime, and its average lifetime is 3.69 ns. Correspondingly, the average lifetimes of OPC and 3PC sample are 2.16 and 2.47, respectively. It can be clearly seen that the lifetime of 2PC sample is significantly stronger than that of OPC and 3PC samples, which indicates that the pyrimidine ring can effectively extend the lifetime of photogenerated carrier, thereby showing the best photocatalytic activity.

In order to explore the influence of electronic properties on the photocatalytic activity of N-containing framework, density functional theory (DFT) calculations are used [48,49]. The density of states (DOS) displays that the OPC, 2PC and 3PC samples have similar band structure composition (Fig. 9 and S10). Among them, the N 2p, O 2p and P 2p states act a leading role in VB and the C 2p state plays a leading role in CB. At the same time, it is calculated that the CB bottom and VB top of 2PC are 0.44 eV and 2.77 eV. The CB bottom and VB top of OPC and 3PC is 0.48 eV and 3.53 eV, 0.45 eV and 2.41 eV, respectively. Interestingly, due to the downward movement of CB, the band gap of 3PC is smaller than that of 2PC and OPC samples, which is in line with the above characterization results. It is worth noting that the dipole of 2PC is 9.46 D, which is larger than the OPC (7.32 D) and 3PC (7.79 D). The larger molecular dipoles in the 2D nanosheets ensure a strong built-in electric field to facilitate photoinduced carrier separation. Therefore, the stronger built-in electric field of 2PC sample significantly enhances the transmission of photoproduced carriers. In addition, according to the literature reported by Kanata et al. [50], it can be obtained that the internal electric field intensity of 2PC is stronger than that of OPC and 3PC samples.

Based on the above analysis, it is reasonable to infer the mechanism of photocatalytic CO₂ reforming to CH₄ in 2PC sample (Fig. 10). Under visible light illumination, 2PC sample can be excited to produce photogenerated electrons in the VB, and the excited electrons are easily transferred to the CB. The reduction process of CH₄ attribute to the following: the electrons can convert CO₂ and H₂O to CH₄; another part of electrons can also convert O₂ to generate O₂^{•−} because the CB potential of 2PC is negative than O₂/O₂^{•−}. The produced O₂^{•−} are easier to reduce with CO₂ to release electrons, which is similar to the mechanism of photocatalytic reduction of Cr⁶⁺ to Cr³⁺ [51,52]. Similarly, this conclusion was confirmed by the capture agent experiment and ESR experiment. Since the electrochemical potential energy of reducing CO₂ to CO (E_{CO₂/CO} = −0.53 eV) is more negative than the CB potential energy of 2PC sample, the gas chromatography did not detect the production of CO.

4. Conclusions

In summary, the cross-linked ultrathin polyphosphazene-based nanosheets with different N-containing skeletons (aromatic ring, pyrimidine ring and s-triazine ring) were constructed through a facile synthesis strategy. By regulated the internal framework, the photon capture performance and CO₂ adsorption capacity in the as-prepared samples can be significantly adjusted. Importantly, constructing a suitable framework can form a strong built-in electric field, which obviously contributes to significantly accelerate the separation of photoproduced carriers. Therefore, the CH₄ evolution rate of 2PC sample reaches 626 μmol g^{−1} (selectivity: near 100%) without the cocatalyst and photosensitizer, which is much higher than many reported photocatalysts. In short, this work provides a fresh method for designing high-performance catalysts through adjusting the polymer framework for highly-selective CH₄ production.

CRedit authorship contribution statement

Guoen Tang: Methodology, Investigation, Formal analysis. **Xiangdong Zeng:** Methodology, Validation. **Linquan Hou:** Methodology, Investigation. **Ting Song:** Writing – review & editing, Funding acquisition. **Shiheng Yin:** Investigation, Formal analysis. **Bei Long:** Methodology, Formal analysis. **Atif Ali:** Visualization, Writing – review & editing. **Guo-Jun Deng:** Writing – review & editing, Funding acquisition.

Declaration of Competing Interest

The authors declare that they have no known competing financial

interests or personal relationships that could have appeared to influence the work reported in this paper.

Acknowledgements

We are extremely grateful for the financial support of the research fund of the Xiangtan University Startup Grant (06KZ/KZ08082), the Science and Technology Innovation Program of Hunan Province (2020RC2076) and the Hunan Provincial Natural Science Foundation of China (2021JJ40529).

Appendix A. Supporting information

Supplementary data associated with this article can be found in the online version at doi:10.1016/j.apcatb.2022.121090.

References

- [1] L. He, W.Y. Zhang, S. Liu, Y. Zhao, Three-dimensional porous N-doped graphitic carbon framework with embedded CoO for photocatalytic CO₂ reduction, *Appl. Catal. B Environ.* 298 (2021) 120546–120557.
- [2] M. Jiang, Y.L. Gao, Z.Y. Wang, Z.X. Ding, Photocatalytic CO₂ reduction promoted by a CuCo₂O₄ cocatalyst with homogeneous and heterogeneous light harvesters, *Appl. Catal. B Environ.* 198 (2016) 180–188.
- [3] S.B. Wang, B.Y. Guan, Y. Lu, X.W. Lou, Formation of hierarchical In₂S₃-CdIn₂S₄ heterostructured nanotubes for efficient and stable visible light CO₂ reduction, *J. Am. Chem. Soc.* 139 (2017) 17305–17308.
- [4] Y.Y. Wang, H.L. Huang, Z.Z. Zhang, C. Wang, Y.Y. Yang, Q. Li, D.S. Xu, Lead-free perovskite Cs₂AgBiBr₆@g-C₃N₄ Z-scheme system for improving CH₄ production in photocatalytic CO₂ reduction, *Appl. Catal. B Environ.* 282 (2021) 119570–119577.
- [5] H. Wu, X.Y. Kong, X.M. Wen, S.P. Chai, E.C. Lovell, J.W. Tang, Y.H. Ng, Metal-organic framework decorated cuprous oxide nanowires for long-lived charges applied in selective photocatalytic CO₂ reduction to CH₄, *Angew. Chem. Int. Ed.* 60 (2021) 8455–8459.
- [6] S.L. Huang, H. Yi, L.H. Zhang, Z.Y. Jin, Y.J. Long, Y.Y. Zhang, Q.F. Liao, J.B. Na, H. Z. Cui, S.C. Ruan, Y. Yamauchi, T. Wakiyama, Y.V. Kaneti, Y.J. Zeng, Non-precious molybdenum nanospheres as a novel cocatalyst for full-spectrum-driven photocatalytic CO₂ reforming to CH₄, *J. Hazard. Mater.* 393 (2020) 122324–122331.
- [7] Z.R. Miao, Q.L. Wang, Y.F. Zhang, L.P. Meng, X.X. Wang, In situ construction of S-scheme AgBr/BiOBr heterojunction with surface oxygen vacancy for boosting photocatalytic CO₂ reduction with H₂O, *Appl. Catal. B Environ.* 301 (2022) 120802–120815.
- [8] X.T. Hu, Z.J. Xie, Q. Tang, H. Wang, L.B. Zhang, J.Y. Wang, Enhanced CH₄ yields by interfacial heating-induced hot water steam during photocatalytic CO₂ reduction, *Appl. Catal. B Environ.* 298 (2021) 120635–120643.
- [9] A. Hayat, N. Shaishta, S.K.B. Mane, A. Hayat, J. Khan, A.U. Rehman, T.H. Li, Molecular engineering of polymeric carbon nitride based donor-acceptor conjugated copolymers for enhanced photocatalytic full water splitting, *J. Colloid Interf. Sci.* 560 (2020) 743–754.
- [10] H. Wang, H. Wang, Z.W. Wang, L. Tang, G.M. Zeng, P. Xu, M. Chen, T. Xiong, C. Y. Zhou, X.Y. Li, D.L. Huang, Y. Zhu, Z.X. Wang, J.W. Tang, Covalent organic framework photocatalysts: structures and applications, *Chem. Soc. Rev.* 49 (2020) 4135–4165.
- [11] W.L. Zhen, J.J. Sun, X.F. Ning, X.Y. Shi, C. Xue, Polymeric carbon nitride with internal n-p homojunctions for efficient photocatalytic CO₂ reduction coupled with cyclohexene oxidation, *Appl. Catal. B Environ.* 298 (2021) 120568–120580.
- [12] X. Wei, D. Zheng, M. Zhao, H.Z. Chen, X. Fan, B. Gao, L. Gu, Y. Guo, J.B. Qin, J. Wei, Y.L. Zhao, G.C. Zhang, Cross-linked polyphosphazene hollow nanosphere-derived N/P-doped porous carbon with single nonprecious metal atoms for the oxygen reduction reaction, *Angew. Chem.* 132 (2020) 14747–14754.
- [13] S. Ali, Z. Zuhra, I.S. Butler, S.U. Dar, M.U. Hameed, D. Wu, L.Q. Zhang, Z.P. Wu, High-throughput synthesis of cross-linked poly(cyclotriphosphazene co-bis (aminomethyl)ferrocene) microspheres and their performance as a superparamagnetic, electrochemical, fluorescent and adsorbent material, *Chem. Eng. J.* 315 (2017) 448–458.
- [14] S. Rothenmund, I. Teasdale, Preparation of polyphosphazenes: a tutorial review, *Chem. Soc. Rev.* 45 (2016) 5200–5215.
- [15] W. Wei, X.B. Huang, X.L. Zhao, P. Zhang, X.Z. Tang, A rapid and efficient strategy for preparation of super-hydrophobic surface with cross-linked cyclotriphosphazene/6F-bisphenol A copolymer microspheres, *Chem. Commun.* 46 (2010) 487–489.
- [16] L.J. Sun, T.H. Liu, H. Li, L. Yang, L.J. Meng, Q.H. Lu, J.G. Long, Fluorescent and cross-linked organic-inorganic hybrid nanoshells for monitoring drug delivery, *ACS Appl. Mater. Interfaces* 7 (2015) 4990–4997.
- [17] J. Byun, W. Huang, D. Wang, R. Li, K.A.I. Zhang, CO₂-triggered switchable hydrophilicity of a heterogeneous conjugated polymer photocatalyst for enhanced catalytic activity in water, *Angew. Chem. Int. Ed.* 57 (2018) 2967–2971.
- [18] Z.J. Zhang, Y.F. Zhu, X.J. Chen, H.J. Zhang, J. Wang, A full-spectrum metal-free porphyrin supramolecular photocatalyst for dual functions of highly efficient hydrogen and oxygen evolution, *Adv. Mater.* 31 (2019) 1806626–1806632.

- [19] Z.J. Zhang, X.J. Chen, H.J. Zhang, W.X. Liu, W. Zhu, Y.F. Zhu, A highly crystalline perylene imide polymer with the robust built-in electric field for efficient photocatalytic water oxidation, *Adv. Mater.* 32 (2020) 1907746–1907752.
- [20] T.J. Yan, L. Wang, Y. Liang, M. Makaremi, T.E. Wood, Y. Dai, B.B. Huang, A. A. Jelle, Y.C. Dong, G.A. Ozin, Polymorph selection towards photocatalytic gaseous CO₂ hydrogenation, *Nat. Commun.* 10 (2019) 2521–2531.
- [21] X.C. Wang, K. Maeda, A. Thomas, K. Takanabe, G. Xin, J.M. Carlsson, K. Domen, M. Antonietti, A metal-free polymeric photocatalyst for hydrogen production from water under visible light, *Nat. Mater.* 8 (2009) 76–80.
- [22] F. Guo, L.J. Wang, H.R. Sun, M.Y. Li, W.L. Shi, High-efficiency photocatalytic water splitting by N-doped porous g-C₃N₄ nanosheets polymer photocatalyst derived from urea and N, N-dimethylformamide, *Inorg. Chem. Front.* 7 (2020) 1770–1779.
- [23] S.B. Wang, Y. Wang, S.L. Zhang, S.Q. Zang, X.W. Lou, Supporting ultrathin ZnIn₂S₄ nanosheets on Co/N-doped graphitic carbon nanocages for efficient photocatalytic H₂ generation, *Adv. Mater.* 31 (2019) 1903404–1903411.
- [24] J.Y. Jiang, W.H. Yang, Y.P. Cheng, Z.D. Liu, Q. Zhang, K. Zhao, Molecular structure characterization of middle-high rank coal via XRD, Raman and FTIR spectroscopy: Implications for coalification, *Fuel* 239 (2019) 559–572.
- [25] K. Ruhlmann, R. Frenzel, R. Horny, A. Nizamutdinova, L. Wüllen, J.M. Will, S. Horn, Investigation of the chemical changes during thermal treatment of polyacrylonitrile and 15N-labelled polyacrylonitrile by means of in-situ FTIR and ¹⁵N NMR spectroscopy, *Polym. Degrad. Stabil.* 146 (2017) 298–316.
- [26] J.Z. Xu, Z.M. He, W.H. Wu, H.Y. Ma, J.X. Xie, H.Q. Qu, Y.H. Jiao, Study of thermal properties of flame retardant epoxy resin treated with hexakis(p-(hydroxymethyl) phenoxy)cyclotriphosphazene, *J. Therm. Anal. Calorim.* 114 (2013) 1341–1350.
- [27] X. Cheng, P.H. Zhao, M. Zhang, S.S. Wang, M.S. Liu, F.S. Liu, Fabrication of robust and bifunctional cyclotriphosphazene-based periodic mesoporous organosilicas for efficient CO₂ adsorption and catalytic conversion, *Chem. Eng. J.* 418 (2021) 129360–129370.
- [28] Z. Jamani, M. Khairuddean, T.G. Seng, A.B. Rahman, Synthesis, characterisation and mesophase transition of hexasubstituted cyclotriphosphazene molecules with schiff base and azo linking units and determination of their fire retardant properties, *Macromol. Res.* 29 (2021) 331–341.
- [29] Y.H. Wang, M.H. Wang, Z.W. Wang, S.M. Wang, J.W. Fu, Tunable-quaternary (N, S, O, P)-doped porous carbon microspheres with ultramicropores for CO₂ capture, *Appl. Surf. Sci.* 507 (2020) 145130–145139.
- [30] P.V. Zinin, L.C. Ming, S.K. Sharma, V.N. Khabashesku, X. Liu, S. Hong, S. Endo, T. Acosta, Ultraviolet and near-infrared Raman spectroscopy of graphitic C₃N₄ phase, *Chem. Phys. Lett.* 472 (2009) 69–73.
- [31] J.S. Singh, FTIR and Raman spectra and fundamental frequencies of biomolecule: 5-Methyluracil (thymine), *J. Mol. Struct.* 876 (2008) 127–133.
- [32] R. Sydam, M. Deepa, A new organo-inorganic hybrid of poly-(cyclotriphosphazene-4,40-bipyridinium)chloride with alarge electrochromic contrast, *J. Mater. Chem. C* 1 (2013) 7930–7941.
- [33] R.J. Waltman, D.J. Pocker, H. Deng, Investigation of a new cyclotriphosphazene-terminated perfluoropolyether lubricant. properties and interactions with a carbon surface, *Chem. Mater.* 15 (2003) 2362–2375.
- [34] Z.D. Zhang, Z.Q. Han, Y.T. Pan, D.H. Li, D.Y. Wang, R.J. Yang, Dry synthesis of mesoporous nanosheet assembly constructed by cyclomatrix polyphosphazene frameworks and its application in flame retardant polypropylene, *Chem. Eng. J.* 395 (2020) 125076–125087.
- [35] N.N. Meng, J. Ren, Y. Liu, Y. Huang, T. Petit, B. Zhang, Engineering oxygen-containing and amino groups into two-dimensional atomically-thin porous polymeric carbon nitrogen for enhanced photocatalytic hydrogen production, *Energy Environ. Sci.* 11 (2018) 566–572.
- [36] P. Edalati, Q. Wang, H.R. Khosroshahi, M. Fujii, T. Ishihara, K. Edalati, Photocatalytic hydrogen evolution on a high entropy oxide, *J. Mater. Chem. A* 8 (2020) 3814–3821.
- [37] M.X. Ji, R. Chen, J. Di, Y.L. Liu, K. Li, Z.G. Chen, J.X. Xia, H.M. Li, Oxygen vacancies modulated Bi-rich bismuth oxyiodide microspheres with tunable valence band position to boost the photocatalytic activity, *J. Colloid Interf. Sci.* 533 (2019) 612–620.
- [38] M.Y. Sun, B.H. Zhao, F.P. Chen, C.B. Liu, S.Y. Lu, Y.F. Yu, B. Zhang, Thermally-assisted photocatalytic CO₂ reduction to fuels, *Chem. Eng. J.* 408 (2021) 127280–127301.
- [39] Z.Z. Yang, J.J. Wei, G.M. Zeng, H.Q. Zhang, X.F. Tan, C. Ma, X.C. Li, Z.H. Li, C. Zhang, A review on strategies to LDH-based materials to improve adsorption capacity and photoreduction efficiency for CO₂, *Coord. Chem. Rev.* 386 (2019) 154–182.
- [40] A.Y. Meng, B. Cheng, H.Y. Tan, J.J. Fan, C.L. Su, J.G. Yu, TiO₂/polydopamine S-scheme heterojunction photocatalyst with enhanced CO₂-reduction selectivity, *Appl. Catal. B: Environ.* 289 (2021) 120039–120050.
- [41] X.W. Zhu, S.Q. Huang, Q. Yu, Y.B. She, J.M. Yang, G.L. Zhou, Q.D. Li, X.J. She, J. J. Deng, H.M. Li, H. Xu, In-situ hydroxyl modification of monolayer black phosphorus for stable photocatalytic carbon dioxide conversion, *Appl. Catal. B Environ.* 269 (2020) 118760–118768.
- [42] L.S. Jiang, J. Li, Y. Li, X.Y. Wu, G.K. Zhang, Promoted charge separation from nickel intervening in [Bi₂O₂]²⁺ layers of Bi₂O₂S crystals for enhanced photocatalytic CO₂ conversion, *Appl. Catal. B Environ.* 294 (2021) 120249–120259.
- [43] Y.B. Wan, D. Meng, X. Zhao, Visible-light-driven H₂O₂ production from O₂ reduction with nitrogen vacancy-rich and porous graphitic carbon nitride, *Appl. Catal. B Environ.* 273 (2020) 119064–119073.
- [44] B. Su, L.J. Huang, Z. Xiong, Y.C. Yang, Y.D. Hou, Z.X. Ding, S.B. Wang, Branch-like ZnS-DETA/CdS hierarchical heterostructures as an efficient photocatalyst for visible light CO₂ reduction, *J. Mater. Chem. A* 7 (2019) 26877–26884.
- [45] S.G. Meng, C. Chen, X.M. Gu, H.H. Wu, Q.Q. Meng, J.F. Zhang, S.F. Chen, X.L. Fu, D. Liu, W.W. Lei, Efficient photocatalytic H₂ evolution, CO₂ reduction and N₂ fixation coupled with organic synthesis by cocatalyst and vacancies engineering, *Appl. Catal. B Environ.* 285 (2021) 119789–119800.
- [46] X.H. Lin, Z.D. Xie, B. Su, M. Zheng, W.X. Dai, Y.D. Hou, Z.X. Ding, W. Lin, Y. X. Fang, S.B. Wang, Well-defined Co₉S₈ cages enable the separation of photoexcited charges to promote visible-light CO₂ reduction, *Nanoscale* 13 (2021) 18070–18076.
- [47] J.Y. Wang, T.T. Bo, B.Y. Shao, Y.Z. Zhang, L.X. Jia, X. Tan, W. Zhou, T. Yu, Effect of S vacancy in Cu₃SnS₄ on high selectivity and activity of photocatalytic CO₂ reduction, *Appl. Catal. B Environ.* 297 (2021), 120498–120508.
- [48] M. Trochowski, M. Kobielusz, K. Mroz, M. Surow, J. Hamalainen, T. Iivonen, M. Leskela, W. Macyk, How insignificant modifications of photocatalysts can significantly change their photocatalytic activity, *J. Mater. Chem. A* 7 (2019) 25142–25154.
- [49] Q. Zhang, H.J. Gu, X.H. Wang, L.F. Li, J.H. Zhang, H.H. Zhang, Y.F. Li, W.L. Dai, Robust hollow tubular ZnIn₂S₄ modified with embedded metal-organic-framework-layers: extraordinarily high photocatalytic hydrogen evolution activity under simulated and real sunlight irradiation, *Appl. Catal. B Environ.* 298 (2021) 120632–120644.
- [50] T.K. Kito, M. Matsunaga, H. Takakura, Y. Hamakawa, T. Nishino, Photorefectance characterization of built-in potential in MBE-produced as-grown GaAs surface, *Proc. SPIE* 1286 (1990) 56–66.
- [51] Y.C. Zhou, X.Y. Xu, P. Wang, H.F. Fu, C. Zhao, C.C. Wang, Facile fabrication and enhanced photocatalytic performance of visible light responsive UiO-66-NH₂/Ag₂CO₃ composite, *Chin. J. Catal.* 40 (2019) 1912–1923.
- [52] C.H. Shen, Y. Chen, X.J. Xu, X.Y. Li, X.J. Wen, Z.T. Liu, R. Xing, H. Guo, Z.H. Fei, Efficient photocatalytic H₂ evolution and Cr(VI) reduction under visible light using a novel Z-scheme SnIn₄S₈/CeO₂ heterojunction photocatalysts, *J. Hazard. Mater.* 416 (2021) 126217–126227.